JOURNAL OF AIRCRAFT
Vol. 48, No. 2, March–April 2011

Computational Evaluation of the Performance of Lifting Surfaces with Leading-Edge Protuberances

Paul W. Weber* and Laurens E. Howle†
Duke University, Durham, North Carolina, 27708-0300
and
Mark M. Murray‡ and David S. Miklosovic§
U.S. Naval Academy, Annapolis, Maryland 21402-5042

DOI: 10.2514/1.C031163

The leading-edge tubercles of humpback whale flippers have been shown to enhance hydrodynamic performance by increasing lift and decreasing drag poststall. To explore this effect, computational simulations of two models based on an idealized humpback whale flipper were conducted, one with a smooth leading edge and one with simulated leading-edge tubercles. Two different commercial computational fluid dynamics packages were used, STAR-CCM+ and SolidWorks Flow Simulation, and the results were compared with experiment. Numeric lift predictions in the nonstall region were reasonably accurate (maximum error 6.6% between both codes), while lift predictions in the poststall region were problematic. Numeric drag predictions in the early nonstall region were within experimental error for STAR-CCM+ using the Spalart–Allmaras turbulence model, while both codes exhibited drag prediction error in the stall region. Flow visualizations showed that the smooth flipper exhibited trailing-edge stall, while the simulated tubercle flipper stalled in the troughs, behind the leading notches, first. At high angles of attack, the simulated tubercle flipper still possessed significant regions of attached flow, which contributes to its ability to maintain increased lift poststall.

Nomenclature

A	=	planform area, cm^2
C_D	=	drag coefficient
C_L	=	lift coefficient
C_P	=	coefficient of pressure
$\bar{c}$	=	mean aerodynamic chord, cm
p_∞	=	freestream pressure, Pa
Re	=	Reynolds Number
U	=	freestream velocity, m/s
x_{LE}	=	chordwise position of the leading edge, in.
x_{TE}	=	chordwise position of the trailing edge, in.
y	=	spanwise coordinate, in
α	=	angle of attack, deg
ρ	=	freestream air density, kg/m^3

I. Introduction

THE motivation for investigating leading-edge (LE) protuberances on fluid dynamic control surfaces stems from the humpback whale (*Megaptera novaeangliae*) flipper, which has rounded tubercles (scallops, sinusoidal perturbations, bumps) interspersed along its LE. Despite its massive length and size, the humpback whale is able to execute complex underwater maneuvers and perform feats such as rolls and loops [1,2]. Since the flippers of the humpback whale are a primary control surface [3], it has been postulated that the LE tubercles on the flippers are major contributors to the humpback whale's underwater agility.

Previous experimental, numerical and theoretical work has been performed to investigate the effects of tubercles on the performance of humpback whale flippers. Watts and Fish [4] conducted the first study related to the unique flipper of the humpback whale, using a panel method to model the tubercles and finding that a wing with leading-edge protuberances may have superior lifting characteristics compared with a wing with a smooth edge. Miklosovic et al. [5] conducted wind-tunnel tests using idealized models of humpback whale flippers and found that the tubercles delay the stall angle by approximately 40% while decreasing drag and increasing lift poststall. Miklosovic et al. [6] conducted a second wind-tunnel study comparing the effect of tubercles on both full-span and semispan models and determined that the tubercles are advantageous for semispan models due to the fact that they inhibit the progression of spanwise stall and create an inherently 3-D flow. Miklosovic et al. [6] further found that tubercles were disadvantageous for full-span models because they caused early flow separation and also resulted in increased drag and decreased lift in the nonstall region. This observation that tubercles are detrimental in the nonstall region for full-span models was also reported by Stein and Murray [7] and Johari et al. [8], although it was also found that in the full-span model case tubercles still contribute to increased lift poststall. Another semispan model finding from wind-tunnel testing was that swept wings with tubercles also exhibit increased lift poststall [9]. A lifting-line model for investigating the effect of tubercles on the stall characteristics of humpback whale flippers was developed by van Nierop et al. [10]. In this study, it was found that tubercles delay stall due to the fact that the trough (valley) sections of the flipper stall at lower angles of attack than the bump (peak) sections due to the influence of upwash in these locales. Though the inviscid 3-D analyses employed by Watts and Fish [4] and van Nierop et al. [10] are inadequate for quantifying the flow separation and stall characteristics of a lifting surface, they do provide valuable information about downwash (and upwash), vorticity distributions, and circulation. These quantities, in turn, provide indications of stall inception and help to validate and interpret the voluminous quantity of computational fluid dynamics (CFD) data. Experimental water-tunnel tests of rudders with leading-edge tubercles by Weber et al.

Received 24 June 2010; revision received 19 September 2010; accepted for publication 8 October 2010.

*Postdoctoral Associate, Department of Mechanical Engineering and Materials Science, Box 90300.
†Associate Professor, Department of Mechanical Engineering and Materials Science, Box 90300.
‡Associate Professor, Mechanical Engineering Department, Mail Stop 11-B.
§Associate Professor, Aerospace Engineering Department, Mail Stop 11-B. Member AIAA.

[11] and of idealized humpback whale flipper models by Stanway [12] confirmed the wind-tunnel results of Miklosovic et al. [5,6] concerning superior poststall performance of the tubercled rudders/models. It was also observed that cavitation first appeared in the troughs for the tubercled rudders [11], indicating low-pressure regions in the troughs, and that flow separates in the troughs first [12].

Pedro and Kobayashi [13] conducted a numerical study of stall delay on humpback whale flippers by simulating the geometry and conditions of the Miklosovic et al. wind-tunnel experiments [5,6]. The commercial CFD code FLUENT with the detached eddy simulation turbulence model was used to simulate both the smooth and scalloped flipper of the Miklosovic et al. [5,6] experiments, and the results were compared with the wind-tunnel data at selected points. Pedro and Kobayashi [13] indicated that the reason the scalloped flipper improves aerodynamic performance is because the tubercles cause streamwise vortices to originate, and these vortices carry momentum to the boundary layer, which delays trailing-edge (TE) separation, and tubercles also confine the leading-edge separation to the tip region.

In this work, the flowfields around the idealized flipper models tested in the wind-tunnel experiments of Miklosovic et al. [5,6] are simulated using two different commercial CFD codes: STAR-CCM+ [14] and SolidWorks Flow Simulation (SFS) 2009 [15]. CFD allows for visualization of the flowfield around the flipper models, which will in turn allow for comparisons between the models in terms of stall characteristics and pressure distributions. Since high-quality experimental data are available, the validity and accuracy of the two different CFD codes will also be explored and compared.

II. Methods

Two different idealized flipper models were tested in this work, one with a smooth LE (baseline flipper) and one with a scalloped LE (simulated tubercle flipper). The two flipper models along with the geometry used in the CFD simulations are pictured in Fig. 1. The baseline and simulated tubercle flipper models were based upon an idealized representation of a humpback whale flipper specimen, which was generated by fitting mathematical functions to the specimen. The construction method and mathematical definitions of the flippers are discussed in Miklosovic et al. [6], but the relevant details will be summarized here. Both models had a mean aerodynamic chord $\bar{c}$ of 13.05 cm (5.086 in.), a span of 56.07 cm (22.50 in.), and a planform area of $A = 737.65$ cm^2 (114.36 in.^{2}). The cross sections of the model were based on a symmetrical NACA 0020 airfoil, although a special cross-sectional transformation was required for the tubercles. A more detailed discussion of the transformation used to generate the tubercles is given in Weber et al. [11]. Equations (1) and (2) were used to define the leading- and trailing-edge planforms for the baseline model (note that the length dimensions of Eqs. (1) and (2) are in inches, consistent with Miklosovic et al. [6]):

$$x_{\mathrm{LE}} = 2.916 + 0.0624y + 0.000428y^2 - 0.000462y^3 \tag{1}$$

$$x_{\mathrm{TE}} = \begin{cases} -3.152 - 0.113y + 0.0194y^2 - 0.000552y^3, & y < 19.98 \text{ in.} \\ -0.374\sqrt{1 - 0.158(y - 19.98)^2} - 1.7, & y \geq 19.98 \text{ in.} \end{cases} \tag{2}$$

In Eq. (1), x_{LE} is the chordwise position that defines the leading edge, x_{TE} is the chordwise position that defines the trailing edge, and y is the spanwise coordinate. The simulated tubercle model was created by applying a sinusoidal profile superposed on the LE contour of the smooth flipper in the spanwise direction, and this profile is defined by Eq. (3):

$$\Delta x_{\mathrm{LE}} = 0.125(1 - 0.001y^2)\sin(0.57y^{1.5} - 0.4)[\tanh(y - 7) + 1] \tag{3}$$

In Eq. (3), all symbols are as defined previously. Equation (3) tapers the amplitude of the sinusoid toward the tip of the flipper and also ensures that A and $\bar{c}$ are equal for the two models. The largest increment generated by Eq. (3) was $\Delta x_{\mathrm{LE}} = \pm 0.223$ in, and it occurred over 39–44% of the span.

The experimental data were collected in the closed-circuit subsonic wind tunnel at the United States Naval Academy and have been published previously [5]. This wind tunnel had a cross section of 137×97 cm and the vented test section has a length of 239 cm [5]. The maximum Mach number achieved during testing was 0.2 (so incompressible flow conditions were assumed), and $Re \approx 505,000$–$520,000$. Finite-wing wind-tunnel corrections were applied to the data [16]. Experimental uncertainty was not more than 0.54% for C_L and 2.5% for C_D. Details of the experimental procedure (including data acquisition procedures) have been extensively documented in previous papers published by the authors [5,6]. The experimental results (along with the corresponding numerical results, to be discussed later) are summarized in Figs. 2–5.

The CFD simulations were conducted using two different commercial codes, STAR-CCM+ [14] and SFS [15] (an add-in to the computer-aided-design program SolidWorks [17]). Two different codes were tested for sake of comparison (especially to see which code, if any, outperformed the other and under what conditions), as each CFD code has its own strengths and weaknesses. Each code solves the Reynolds-averaged Navier–Stokes (RANS) equations [18] on a finite volume mesh using a turbulent flow model (laminar and inviscid models were also available for both codes but not used). Convergence studies were conducted for each code (to be described later), although in the deep-stall regions machine memory (which controls mesh size) became an issue. The same geometry and dimensions that were present in the experiment were used for the simulation (no mesh scaling was performed; see Fig. 1). Additionally, the experimentally recorded flow conditions were used as parameters in the simulations, which were a temperature of $T = 318$ K, a far-field flow speed of $U = 69.6$ m/s, and an air density of $\rho = 1.103$ kg/m^3. The geometry for the simulations was generated in SolidWorks and then was either used directly (for SFS, which interfaces directly with SolidWorks) or was imported into the CFD program (STAR-CCM+). Steady flowfield simulations were used in the early nonstall region for both of the flippers, although when the flowfield became more complex in the stall region, it was necessary to run unsteady flowfield simulations for better accuracy.

The time step for the unsteady simulations was calculated by dividing a characteristic length (the wind-tunnel test section length of 1.8 m) by U, which gives a characteristic particle travel time through

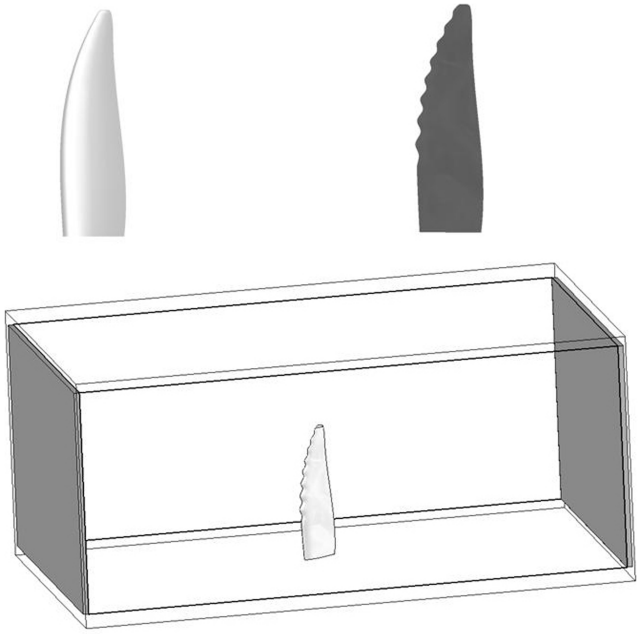

Fig. 1 Geometry for experiment and simulation: smooth (baseline) flipper (top left), simulated tubercle (scalloped) flipper (top right), representative flipper model in wind-tunnel test section (bottom).

Table 1 Time-step study results for STAR-CCM+[a]

Time step	Iterations	Time steps	Physical time, s	C_L	C_D
Steady	1700	N/A	N/A	0.147	0.0139
2.59×10^{-5} s	111,902	5594	0.1448846	0.142	0.0104
5.18×10^{-5} s	45,461	2272	0.1176896	0.142	0.0105
1.036×10^{-4} s	46,460	2322	0.2405592	0.142	0.0105

[a]Tubercle flipper, $\alpha = 2°$, and Spalart–Allmaras model.

the tunnel. This number was then divided by 1000 to give the unsteady time step of 2.59×10^{-5} s. A time-step study was conducted to determine the effect of altering the time step from this calculated value, the results of which are presented in Tables 1 and 2. It was found that decreasing the time step to 1.036×10^{-5} s had no significant effect on solution accuracy. Therefore, this larger value of time step was used for all calculations in order to decrease solution convergence time.

SFS simulations were run on a 64-bit Windows-based machine with a 2.66 GHz processor and 32 GB of RAM. SFS features automatic mesh generation, which is advantageous in terms of simplicity but disadvantageous in terms of user ability to control mesh features. SFS constructs the basic mesh by dividing the computational domain into slices by parallel planes that are orthogonal to the global coordinate system's axes [15]. For near-wall treatment, the local initial mesh feature of SFS was used on the flipper model, which ensures better resolution of the model-specific geometry in the local region of the computational domain specified (i.e., the fluid area around the flipper). The k-ε turbulence model is the only turbulence model available in SFS to close the flowfield equations; the default turbulence parameter values in the model were used [15] and are listed in Table 3. SFS also features solution adaptive mesh refinement, where the code increases the mesh density in areas of high gradients and decreases mesh density in areas of low gradients when directed during the simulation, and possesses multiprocessor solver capability.

STAR-CCM+ simulations were run on a Linux-based server with eight 2.3 GHz processors and 32 GB of RAM. STAR-CCM+ features multiple mesh types (polyhedral, tetrahedral, and trimmer), all of which require the user to generate a surface mesh on the geometry of interest, which is then the basis for the volume mesh. The prism-layer meshing feature of STAR-CCM+ was used for near-wall meshing. The prism-layer mesh is composed of orthogonal prismatic cells that reside next to wall boundaries and is required to accurately simulate turbulence [14]. Five total prism layers were used. The polyhedral meshing model was used for all STAR-CCM+ simulations due to its increased accuracy and performance characteristics (a polyhedral mesh requires 4 times fewer cells, half the memory and a fifth of the computing time of a tetrahedral mesh) and superior convergence properties [14]. STAR-CCM+ automatically ensures smooth transition between the prism-layer mesh and the polyhedral mesh. Multiprocessor computing is supported by the STAR-CCM+ flow solver, which significantly reduces computation time. Four different turbulence models are available in STAR-CCM+: Spalart–Allmaras, k-ε, k-ω, and Reynolds stress. The one-equation Spalart–Allmaras model was chosen for simulations in the nonstall region where boundary layers are attached and separation is mild, whereas the more robust two-equation k-ω model was chosen for simulations in the stall region [18]; the effect of turbulence model choice and reasons for these particular model choices will be discussed in Sec. III. Default parameters for the turbulence models were used [14] and are defined in Table 3.

Table 2 Turbulence model study results for STAR-CCM+[a]

Model	C_L[b] (% error)	C_D[c] (% error)
k-ε	0.490 (7.7)	0.0303 (53.8)
k-ω	0.483 (6.2)	0.0297 (50.8)
Spalart–Allmaras	0.475 (4.4)	0.0230 (16.8)

[a]Tubercle flipper, $\alpha = 6°$, and steady solver.
[b]Experimental value of 0.455.
[c]Experimental value of 0.0197.

Data are reported in terms of the coefficients of lift and drag,

$$C_{L,D} = \frac{2F_{L,D}}{\rho U^2 A} \tag{4}$$

where $F_{L,D}$ is the measured (either experimentally or numerically) lift and drag force and all other symbols are defined in the Nomenclature. The coefficient of pressure is defined as

$$C_P = \frac{2(p - p_\infty)}{\rho U^2} \tag{5}$$

where p is the pressure at a point of interest and all other symbols are defined in the Nomenclature.

III. STAR-CCM+ Results and Experimental Comparison

A. Convergence Study and Numeric Errors

Different mesh sizes were necessary for convergence in STAR-CCM+ depending on whether the simulations were performed in the stall or nonstall region. For the nonstall region, 900,000 polyhedral cells was the converged solution mesh size for both the smooth and tubercle flippers. To give an example of how this number was obtained, for the smooth flipper at $\alpha = 6°$, when the mesh size was increased from 848,460 polyhedral cells to 1,045,475 polyhedral cells, C_L changed 3.8%, and C_D changed 1.1%. Additionally, as to be discussed later, the converged solutions in the nonstall region were found to agree closely with the experiment. This stands in stark

Table 3 Turbulence model parameters for SFS and STAR-CCM+

Parameters	Values
SolidWorks Flow Simulation, k-ε model	
Turbulence intensity I_t	0.5%
Turbulence length L_t	0.42 in.
STAR-CCM+, k-ε model	
$C_{\varepsilon 1}$	1.44
$C_{\varepsilon 2}$	1.92
C_μ	0.09
σ_k	1.0
σ_e	1.3
C_t	1
STAR-CCM+, k-ω model	
β^*	0.09
β	9/125
α	13/25
α^*	1
σ_k	0.5
σ_w	0.5
STAR-CCM+, Spalart–Allmaras model	
C_{v1}	7.1
C_{prod}	2.0
C_{b1}	0.1355
C_{b2}	0.622
C_{w2}	0.3
C_{w3}	2.0
κ	0.41
$\sigma_{\tilde{v}}$	2/3

contrast to the stall region, where the convergent mesh size was found to be highly dependent on flipper type and degree of stall. At the onset of stall, mesh sizes of 1,800,000 polyhedral cells for the tubercle and smooth flipper were found to yield converged solutions that agreed closely with the experiment. However, in the deep-stall region (past $\alpha = 18°$ for the tubercle flipper and $\alpha = 14°$ for the smooth flipper), the machine limit of $\sim 2,000,000$ polyhedral cells was a limitation and prevented further mesh studies. As an example, for the smooth flipper at $\alpha = 16°$, when the mesh was increased from 1,367,849 to 1,945,879 polyhedral cells, C_L changed 2.4%, and C_D changed 2.4%. It must be acknowledged that significant convergence may remain when grid adaptation hits its limit, but, as previously mentioned, hardware limitations prevented further mesh studies.

To test the resultant numeric error involved in the simulation, the residuals were tracked in STAR-CCM+. The STAR-CCM+ documentation [14] defines the residual as the degree to which the discretized equation is not completely satisfied. A perfectly converged solution would have a residual in each cell equal to machine round-off. Since the residuals are summed over each cell, the absolute magnitude of the residual (which depends upon the number of cells) was not as useful a quantity to track as ensuring that the residual stopped changing over time. The change in residual was taken as the criteria for convergence. The residuals converged for all simulations conducted in STAR-CCM+. Typical numeric values for the continuity residual were less than 0.001 for a simulation with approximately 900,000 cells and less than 0.01 for a simulation with approximately 2,000,000 cells, which demonstrates the point mentioned previously that the absolute value of the residual may change significantly (sometimes by orders of magnitude) based on the size of the mesh.

B. Effect of Turbulence Model in STAR-CCM+

As mentioned previously, there are four turbulence models available in STAR-CCM+: Spalart–Allmaras, k-ε, k-ω, and Reynolds stress. To test the effect of varying the turbulence model, a characteristic simulation (tubercle flipper, $\alpha = 6°$, and steady solver) was chosen and the turbulence model was varied. The Reynolds stress turbulence model was not tested due to the extreme computational power required (Reynolds stress model is the most computationally expensive of the turbulence models listed). The results of this study are shown in Tables 1 and 2. The Spalart–Allmaras model is seen to have the least error in C_L (4.4%), with the k-ε model exhibiting the maximum error in C_L (7.7%). All of the models exhibited significant error in predicting C_D (minimum error Spalart–Allmaras at 16.8%, maximum error k-ε at 53.8%), but it is of note that the predicted C_D for the Spalart–Allmaras model was within the experimental uncertainty range. It was found that at higher values of α characterized by flow separation and stall effects, the Spalart–Allmaras model diverged. Therefore, for the STAR-CCM+ simulations conducted in this work, the Spalart–Allmaras model was used for small α, whereas the next-best-performing k-ω model was used for higher α.

C. STAR-CCM+ Smooth Flipper Predictions Versus Experiment

The C_L-vs-α curves for the experimental and CFD smooth flipper trials are presented in Fig. 2. Agreement of the STAR-CCM+ CFD results with the experimental data is qualitatively excellent in the nonstall region (α up to 12°), with the maximum error at 3.6% for $\alpha = 8°$. Because of the very small experimental uncertainty, the quantitative value of most of the predicted data points fell outside the uncertainty band. The Spalart–Allmaras turbulence model was valid up to $\alpha = 6°$, after which the onset of flow separation required use of the k-ω model for all higher α. The steady flow solver yielded accurate results up to $\alpha = 12°$ (the very beginning of the onset of stall), after which point the unsteady flow solver was required. In the stall region ($\alpha = 14$, 16, and 18°), STAR-CCM+ overpredicted the value of C_L and also missed the stall point by 4° ($C_{L,\max}$ was experimentally found to occur at approximately 12°, whereas the simulation predicted stall at approximately 16°).

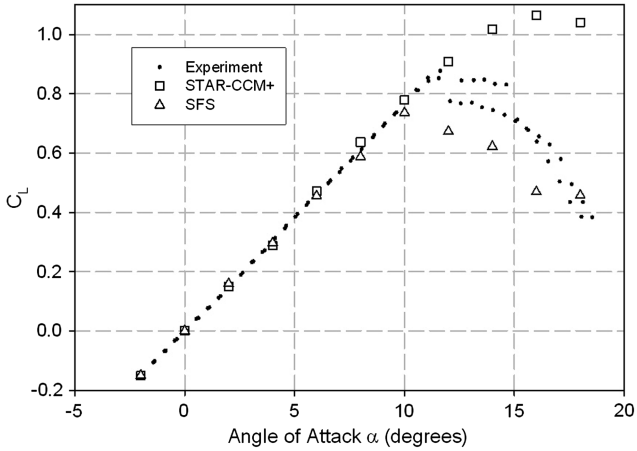

Fig. 2 Smooth flipper lift coefficient C_L versus angle of attack α for the experimental and CFD trials. The size of the experimental data points corresponds to the magnitude of the experimental uncertainty. Both codes are seen to predict C_L with reasonable accuracy in the nonstall region ($\alpha < 12°$), while STAR-CCM+ overpredicts C_L poststall and SFS generally underpredicts C_L poststall.

The experimental and CFD smooth flipper C_D-vs-α curves are presented in Fig. 3. For STAR-CCM+, a stark contrast between turbulence models in terms of drag prediction is evident, as the C_D predictions of the Spalart–Allmaras model (α up to 6°) were again excellent (and this time, due to the larger uncertainty in C_D, the predicted points fell within the experimental uncertainty band up to $\alpha = 6°$), whereas the k-ω model overpredicted C_D for $\alpha = 8$ and 10° and underpredicted C_D for α higher than 14° (the 12° prediction was qualitatively close to the experiment). Difficulties in predicting C_D for complex, stalled flows were especially evident at the highest α of 18°, where the predicted C_D was only 62% of its experimental value with the machine-limit mesh size.

D. STAR-CCM+ Tubercle Flipper Predictions Versus Experiment

The C_L-vs-α curves for the experimental and CFD tubercle flipper trials are presented in Fig. 4. STAR-CCM+ predictions of C_L for low and moderate values of α (up to 14°) were qualitatively decent, with the maximum error in this range being 6.6% at $\alpha = 10°$. The quantitative predictions were outside of the experimental uncertainty bands. The tubercle flipper required transition from the Spalart–Allmaras turbulence model to the k-ω model at a smaller α (6°) than the smooth flipper (8°), at which point it was also necessary to use the

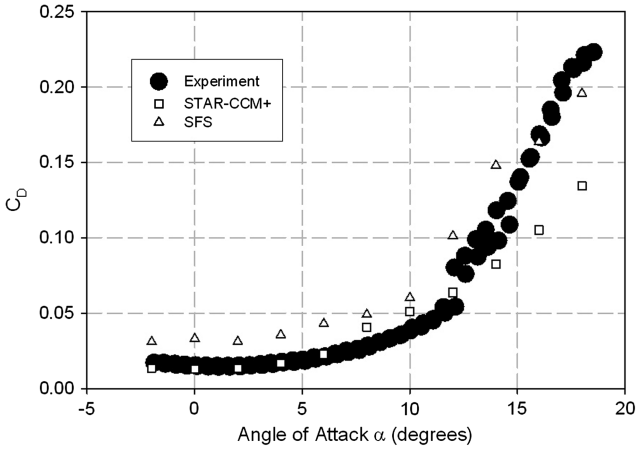

Fig. 3 Smooth flipper drag coefficient C_D versus angle of attack α for the experimental and CFD trials. The size of the experimental data points corresponds to the magnitude of the experimental uncertainty. STAR-CCM+ predicts C_D to within experimental uncertainty for $\alpha \leq 6°$ and $\alpha = 12°$, overpredicts C_D for $\alpha = 8$ and 10°, and underpredicts C_D for $\alpha \geq 14°$. SFS significantly overpredicts C_D for all α up until the deep-stall region ($\alpha \geq 16°$).

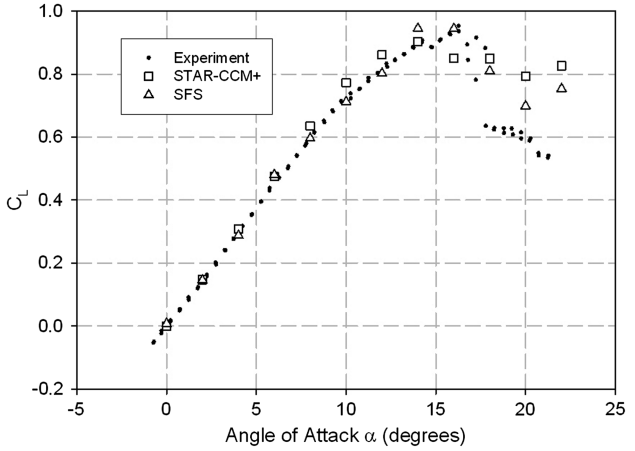

Fig. 4 Tubercle flipper lift coefficient C_L versus angle of attack α for the experimental and CFD trials. The size of the experimental data points corresponds to the magnitude of the experimental uncertainty. STAR-CCM+ predicts C_L well up until $\alpha = 8°$, overpredicts C_L until $C_{L,\max}$ is reached, then both over and underpredicts C_L depending on α in the stall region. SFS predicts C_L well up until $\alpha = 12°$, then overpredicts C_L for all greater α.

unsteady flow solver. As noted by Miklosovic et al. [6], an α of 6° for the tubercle flipper is where the lift-curve slope changes (decreases; see Fig. 4) and characteristic unsteadiness in the flow is introduced; therefore, it is not surprising that the unsteady flow solver and k-ω turbulence model were required at the vicinity of this point and beyond. C_L was underpredicted $\alpha = 16°$. At $\alpha = 18°$, the predicted C_L value was within a reasonable experimental range (the experiment showed a sharp drop in C_L at approximately $\alpha = 18°$). For the highest α of 20 and 22°, the CFD code overpredicted the value of C_L with a mesh at the machine-limit size, though not nearly as much as it did for the smooth flipper (the simulation value was approximately 53% greater than the experimental value at $\alpha = 22°$).

The experimental and CFD tubercle flipper C_D-vs-α curves are presented in Fig. 5. A similar trend to that of the smooth flipper for STAR-CCM+ was evident, where C_D for the Spalart–Allmaras model was in close agreement to the experiment (i.e., within the experimental uncertainty bands due to the larger uncertainty in C_D) for all values of α in its operational range (up to $\alpha = 6°$). In the range of $\alpha = 8$–14°, the k-ω model overpredicted C_D. The k-ω predicted value of C_D is within the experimental uncertainty at $\alpha = 16°$. At all points past this ($\alpha = 18, 20, 22°$), C_D is underpredicted. Once again, underprediction of C_D in the stall region for the tubercle flipper was

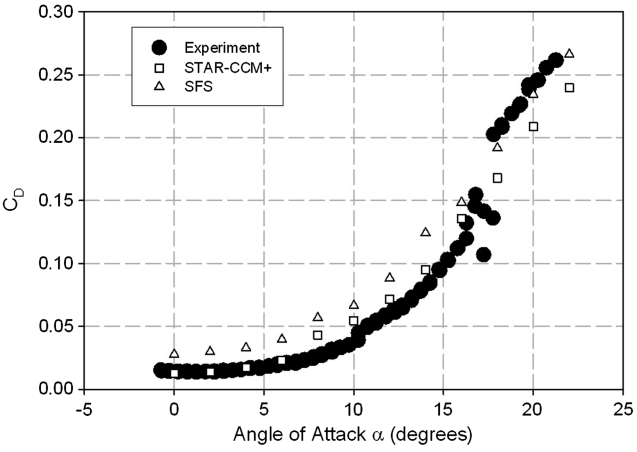

Fig. 5 Tubercle flipper drag coefficient C_D versus angle of attack α for the experimental and CFD trials. The size of the experimental data points correspond to the magnitude of the experimental uncertainty. STAR-CCM+ predicts C_D to within experimental uncertainty for $\alpha \leq 6°$, overpredicts C_D for $\alpha = 8$–16°, then underpredicts C_D for $\alpha \geq 18°$. SFS overpredicts C_D for $\alpha \leq 16°$ then underpredicts C_D for $\alpha \geq 18°$.

not as dramatic as it was for the smooth flipper; for example, the predicted value of C_D at $\alpha = 20°$ was 85% of the experimental value.

Overall, STAR-CCM+ C_L predictions were reasonable in the nonstall region for both flipper models. In contrast, STAR-CCM+ overpredicted C_L in the stall region for both flipper models. The quality of C_D predictions in STAR-CCM+ was found to depend upon the turbulence model. In the nonstall region, using the Spalart–Allmaras turbulence model with STAR-CCM+ resulted in C_D predictions that were within experimental uncertainty. In regions with slight (pre-$C_{L,\max}$) and massive (post-$C_{L,\max}$) flow separation, which necessitated using the k-ω turbulence model, STAR-CCM+ was found to overpredict C_D pre-$C_{L,\max}$, whereas it underpredicted C_D post-$C_{L,\max}$.

IV. SolidWorks Flow Simulation Results and Experimental Comparison

A. SFS Convergence Study and Numeric Errors

Different mesh sizes were necessary for convergence in SFS depending on whether the simulations were performed in the stall or nonstall region. For the nonstall region, 1,200,000 cells was the converged solution mesh size for both the smooth and tubercle flippers. To give an example of how this number was obtained, for the smooth flipper at $\alpha = 4°$, when the mesh size was increased from 1,123,344 cells to 1,438,440 cells, C_L changed 0.8% and C_D changed 3.3%. In the near-stall and poststall regions (past $\alpha = 8°$ for the tubercle flipper and $\alpha = 12°$ for the smooth flipper), the machine limit of 2,300,000 cells was a limitation. As an example, for the tubercle flipper at $\alpha = 20°$, when the mesh was increased from 1,453,151 to 2,312,888 cells, C_L changed 10.8% and C_D changed 3.2%.

Numeric errors in SFS are calculated using an internal algorithm. The user specifies goals, which are parameters of interest for the calculation (the lift coefficient and drag coefficient for this work). According to the SFS documentation [17], when SFS analyzes a goal's convergence, it calculates the goal's dispersion, which is defined as the difference between the goal's maximum and minimum values over the analysis interval reckoned from the last iteration and compares this dispersion with the goal's convergence criterion dispersion. This convergence criterion dispersion may be specified by the user, but by default it is specified automatically and that is what was done for this work. Some care must be taken with this automatic convergence criteria; most notably, for unsteady simulations, it was ensured that at least one characteristic time was calculated before the simulation was allowed to terminate by the convergence criteria.

B. SFS Smooth Flipper Predictions Versus Experiment

Agreement between the SFS CFD results and the experimental data (Fig. 2) is acceptable in most of the nonstall region (α up to 10°), with the greatest difference between experiment and CFD occurring at $\alpha = 10°$ (3.5% error). However, due to the very small experimental uncertainty, the quantitative value of most of the predicted data points fell outside the uncertainty band. The steady flow solver yielded accurate results up to $\alpha = 10°$, after which point the unsteady flow solver was required. Near $C_{L,\max}$ and in most of the stall region ($\alpha = 12$–16°), SFS underpredicted the value of C_L. However, at the deep-stall point of $\alpha = 18°$, the predicted SFS value was within 5% of the experimental value. SFS correctly predicted the onset of stall effects at 12° (the experimental data shows hysteresis at this point), although as mentioned previously SFS underpredicted the numerical value of C_L.

SFS is seen to overpredict C_D for all α from −2 to 14° (Fig. 3), with the maximum overprediction being 224% at $\alpha = 0°$. Curiously, in this range, the absolute numerical value of the C_D overprediction appears to be relatively constant, i.e., the predicted drag curve is qualitatively the same shape as the experimental curve and it differs from the experimental curve by an additive constant. At $\alpha = 16°$, the SFS C_D prediction is within the experimental uncertainty band. At the highest α of 18°, SFS transitions from overpredicting C_D to underpredicting C_D (9.3% error).

C. SFS Tubercle Flipper Predictions Versus Experiment

SFS predictions of C_L (Fig. 4) over low and moderate values of α (up to $C_{L,\max}$) were qualitatively reasonable, with the maximum error in this range being 5.5% (overprediction) at $\alpha = 14°$. At $\alpha = 18°$, the predicted C_L value was within a reasonable experimental range (as noted previously, the experiment showed a sharp drop in C_L around $\alpha = 18°$ so the experimentally measured value of C_L varies around this α). For the highest α of 20 and 22°, SFS overpredicts the value of C_L with a mesh at the machine-limit size, which differs from the smooth flipper where SFS underpredicted C_L at deep stall.

The experimental and CFD tubercle flipper C_D-vs-α curves are presented in Fig. 5. A similar trend to that of the smooth flipper for SFS was evident, where C_D in the range of $\alpha = 0$–16° was overpredicted (maximum overprediction was 217% at 2°). As before, the predicted drag curve is qualitatively similar in shape to the experimental drag curve and appears to differ only by an additive constant. The predicted value of C_D actually improves at higher α(18°, 20°, 22°) in comparison with experiment. As with the smooth flipper, SFS tends to underpredict C_D in the deep-stall region, although the error was relatively small at 3.2%.

Overall, SFS gave reasonable C_L predictions in the nonstall region for both flipper models. C_L was overpredicted in the stall region for the tubercle flipper but underpredicted in the stall region for the smooth flipper. C_D predictions were problematic in the nonstall region, sometimes being off by more than a factor of 2 and overall were also problematic in the stall region (with the exception of some individual data points). Because of the fact that only one turbulence model is available in SFS (k-ε), it was not possible to test if C_D predictions would improve with utilization of a different turbulence model.

V. Comparison of STAR-CCM+ and SolidWorks Flow Simulation

In this section, the two CFD codes STAR-CCM+ and SFS will be compared. The advantages of each code will be discussed first, and the section will conclude with observations and recommendations regarding the two codes.

A. STAR-CCM+ Advantages

One of the main advantages of STAR-CCM+ is the fact that multiple turbulence models are available, which was especially important in terms of predicting drag. The fact that STAR-CCM+ predicted drag accurately for low angles of attack for both flippers (Figs. 3 and 5) is due to the fact that the Spalart–Allmaras model was

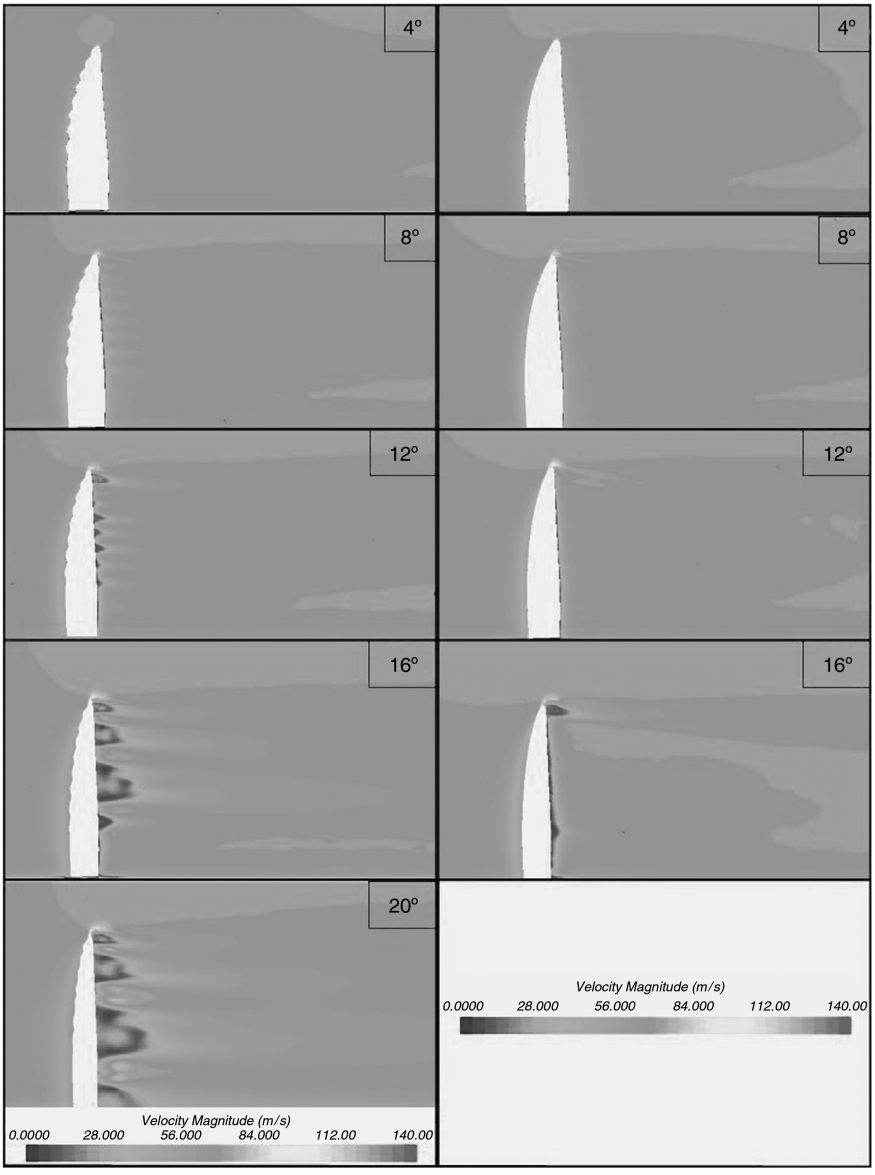

Fig. 6 Velocity profiles for the tubercle (left column) and smooth (right column) flippers. Cut plane was taken parallel to the freestream flow direction through the center of the tunnel. The velocity magnitude is reported. Results were generated using STAR-CCM+.

available. Different turbulence models are suitable for different types of flows, and the ability to change between them is a marked advantage. Both STAR-CCM+ and SFS offer the user the ability to change the default parameters of the turbulence models (given in Table 3), although we did not change the default turbulence parameters in this study. The reasons for this were twofold. First, we desired to compare the two codes in their default states. Second, we had experimental results for comparison and could have modified the turbulence model parameters to give more accurate CFD results. However, CFD is most frequently used as a predictive tool for situations where experimental measurements are not available. In a case such as this, unless the special knowledge were available regarding the flow state, the default turbulence parameters would most likely be used.

Another advantage of STAR-CCM+ lies in meshing, which is an important factor in any CFD calculation. As mentioned previously, STAR-CCM+ features a polyhedral mesh, which gives more accurate results than a tetrahedral mesh of the same size (although tetrahedral and trimmer meshes are also available if desired). STAR-CCM+ also allows (in fact, requires) the user to have detailed control over the mesh generation, allowing for greatly increased mesh density in areas of interest and specifying mesh parameters near solid boundaries. In contrast, SFS uses a rectangular prism mesh, which is automatically generated. SFS does allow the user to specify areas where increased mesh density is desired, although not to the same degree as STAR-CCM+.

B. SFS Advantages

The principal advantage possessed by SFS is simplicity of use. Setting up the simulation in SFS was much faster than doing so in STAR-CCM+ (since it was tied in with the CAD program used to create the simulation), and many features that required careful user attention in STAR-CCM+ were automatically taken care of in SFS. For example, as noted previously, mesh generation in SFS is automatic, so although the user does sacrifice some control over mesh details, the user also does not have to spend a great deal of time generating the mesh. Additionally, the meshes generated by SFS were of high quality, whereas in STAR-CCM+ a divergent mesh could easily be generated if the user was not careful. SFS is also able to self-diagnose some potential calculation problems; for example, warnings are given on the solver interface during the calculation if certain criteria are violated such as using a time step that is too large.

STAR-CCM+ and SFS each had their individual strengths and weaknesses as CFD codes, and for this study it was found that the flow conditions determined which code was superior. The deciding factor in determining which code is superior was accuracy of numerical predictions when compared with experiment. The following recommendations are made:

1) For simulations at low α in the nonstall region, characterized by little or no flow detachment, STAR-CCM+ with the Spalart–Allmaras turbulence model is the recommended code due to accurate prediction of both C_L and C_D.

2) For simulations at moderate α (but less than α at $C_{L,\max}$), characterized by some flow detachment but not yet in the stall region, STAR-CCM+ with the k-ω turbulence model is the recommended code due to decent prediction of C_L and C_D.

3) For simulations at high α in the stall region, characterized by flow detachment, SFS is the recommended code due to superior C_L predictions and slightly better C_D predictions (although C_D predictions for both codes were problematic in the stall region, so neither code did particularly well).

Since the two codes were run on different platforms (i.e., Linux vs Windows) and used different mesh types, no attempt will be made to compare the relative computation speed of the two codes.

VI. Discussion

In the Discussion section to follow, the differences in stall mechanisms and pressure distributions between the two flippers will be explored.

A. Differences in Stall Mechanisms

To investigate the differences in the stall mechanisms between the two flipper models, flow visualizations were created from the CFD results. Figure 6 shows velocity profiles for the two flippers that were generated with STAR-CCM+ by considering a cut plane parallel to the freestream flow direction running through the center of the tunnel, with the velocity magnitude reported. Figure 7 is a visualization of the fluid flowpath lines for the tubercle and smooth flippers, generated using SFS.

The stall mechanism for the tubercle flipper (Figs. 6 and 7) will be discussed first. For the low α of 4 and 8°, flow over the flipper was seen to be smooth with minimal velocity deficit in the wake. At the onset of stall ($\alpha = 12°$), separation occurred at the root of the flipper near the wall and behind one of the troughs at 75% of the half-span (Fig. 7). Additionally, a velocity deficit in the wake was beginning to form downstream of the troughs as evidenced by striations in the velocity distribution that correspond to the spanwise position of each trough (Fig. 6). When α was increased to 16°, the separation region behind the trough that was present at $\alpha = 12°$ had grown larger (Fig. 7), with the flipper now partially stalled, and low values of

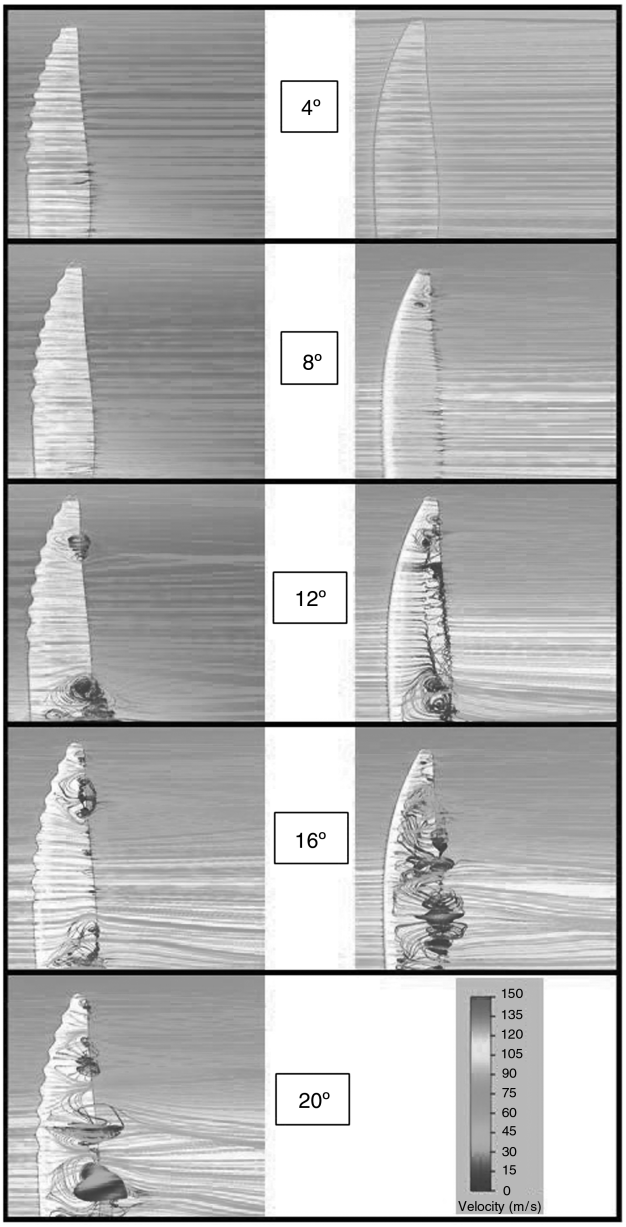

Fig. 7 Fluid flowpath-line comparison between the smooth (right column) and tubercle (left column) flippers at select angles of attack. Results were generated with SFS.

velocity were seen along much of the TE. The velocity deficit in the wake had also grown in size (Fig. 6), with four distinct regions present: a smaller region near the tip, two large regions along the span behind the tubercles, and one smaller region behind the trough of the tubercle nearest to the root. In deep stall ($\alpha = 20°$), there were three large flow separation regions on the flipper, one at the root and two along the span behind the tubercles (Fig. 7), and multiple smaller ones (especially at the tip). Also, it appeared that the major flow separation region near the tip at $\alpha = 20°$ had shifted toward the root and was centered behind a different trough than the major tip stall region at $\alpha = 16°$. In the wake, the velocity deficit had become prominently larger at $\alpha = 20°$ (Fig. 6), with two of the major velocity-deficit regions at $\alpha = 16°$ combining into one at $\alpha = 20°$, along with a new major velocity-deficit region near the root. This phenomenon of the tubercles first causing stall behind the troughs was noted in the airfoil experimental flow visualization work of Johari et al. [8] and the water-tunnel experiments of Stanway [12]. The stalling in the trough regions can be explained by analyzing the downwash/upwash distributions induced by the tubercles. Each tubercle effectively modeled a small delta wing having a 45° LE sweep, with a rounded apex and a large airfoil LE radius. Such a geometry induced a separation flowfield with a leading-edge vortex on the upper (suction) surface of the tubercle. Therefore, the flowfield produced a net downwash over the spanwise position of each peak and a net upwash over the spanwise position of each trough. Localized upwash in the trough regions generated locally higher effective angles of attack, more severe adverse pressure gradients, and early separation compared with the peak regions. This is similar to the assessment of Pedro and Kobayashi [13], as their numerical results demonstrated that the tubercle flipper displayed large streamwise vortices aligned with the tubercles. The streamline patterns at midspan in Fig. 7 are evidence of the presence of downwash and upwash. It is this presence of vorticity that suppressed the same level of large-scale flow separation that characterized the smooth flipper.

We will now shift the focus of our discussion to the stall mechanism for the smooth flipper (Figs. 6 and 7). For the low α of 4 and 8°, flow over the flipper was again seen to be smooth with minimal velocity deficit in the wake, although flow separation was beginning to form near the tip at 8°. When α was increased to 12° (which was near the maximum C_L), the flow separation region at the tip of the flipper had grown larger, and trailing-edge stall was developing along most of the trailing edge of the flipper (Fig. 7). A distinct stall line at $\alpha = 12°$ was also seen in the middle portion of the smooth flipper, from about 20–80% of the half-span. Velocity deficit in the wake had not significantly developed yet at $\alpha = 12°$ because of the inception of a type-I turbulent flow stall pattern (Fig. 6). Full flow separation had not yet occurred. However, when α was increased to 16°, which is in the stall region, a large region of flow separation had developed across the entire flipper (Fig. 7). The trailing-edge stall evident at $\alpha = 12°$ was also seen to have fully developed into a large region at this higher α. In this stalled condition, the velocity deficit in the wake had developed across the entire trailing edge of the flipper (Fig. 6). These CFD flow visualization results were again similar to the experimental flow visualization results of Johari et al. [8], who found that when compared with a tubercled airfoil, a nontubercled (i.e., smooth) airfoil tends to stall from the trailing edge first, and the stall progresses toward the leading edge as α is increased. Our results are in agreement with Pedro and Kobayashi [13], who found a TE type of flow separation common to both geometries and also noted propagation of stall toward the root (Fig. 7).

In addition to showing qualitative differences in the stall mechanisms between the smooth and tubercle flippers, these flow visualizations also give a qualitative explanation as to why the tubercles delay stall. For the smooth flipper, once stall was obtained, the entire trailing edge was stalled with progressively massive flow separation and velocity deficits existing in the wake (Figs. 6 and 7). However, for the tubercle flipper, even when the flipper was in deep stall, there were still regions along the flipper span where the flow was largely attached (Figs. 6 and 7), which resulted in a higher C_L poststall.

B. Differences in Pressure Distribution

The CFD results were used to visualize the differences in the pressure distribution on the surfaces of the two flippers, and the results are presented in Fig. 8. Numeric values of the pressure at the second tubercle and second trough from the root toward the tip are also presented in Fig. 8. For the tubercle flipper at the low, nonstall α of 4 and 8°, the contours were generally seen to run in the spanwise direction, the pressure gradients were more severe in the troughs, and the lowest global value of pressure occurred in the troughs. The quantitative values of pressure given in Fig. 8 for the representative trough and tubercle also show that the pressure was lower in the

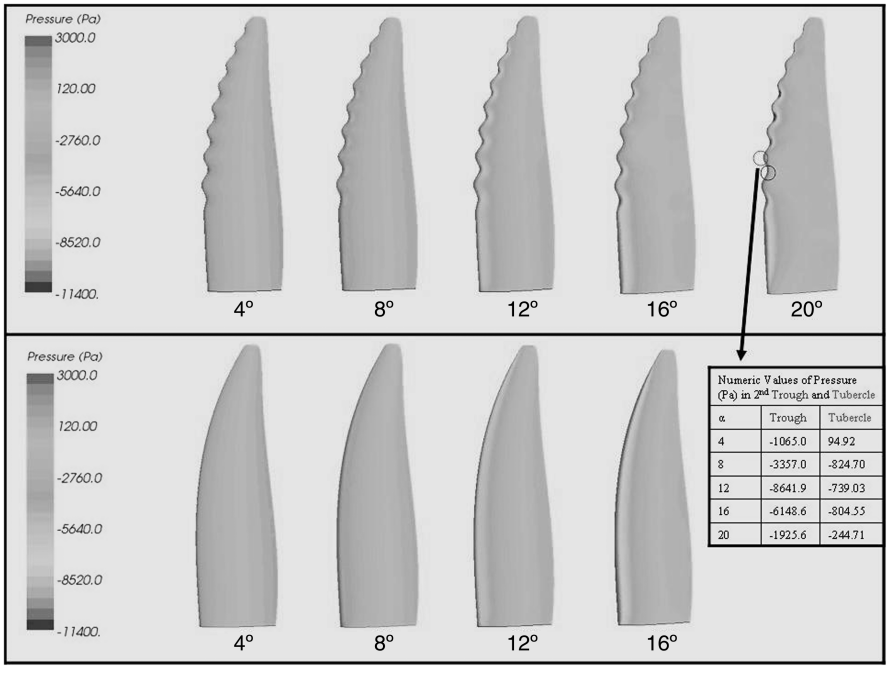

Fig. 8 Surface pressure contours for the tubercle (top) and smooth (bottom) flippers. All pressures are reported with respect to a reference pressure of 0.0 Pa. Freestream velocity is left to right (i.e., the suction side of the flipper is shown). Results were generated with STAR-CCM+.

trough then on the tubercle. The fact that the pressure gradients are more severe in the troughs was indicated by van Nierop et al. [10] as the reason why stall develops first there. This is also the consequence of the downwash/upwash distributions induced by the sinusoidal tubercle LE planform. In fact, the tubercle flippers at α of 4 and 8° in Fig. 8 look qualitatively similar to the theoretically calculated pressure contour for a humpback whale flipper presented as a figure in the work of van Nierop et al. [10]. When α for the tubercle flipper was increased to 12°, the pressure gradient in the troughs was seen to become more severe, the lowest global value of pressure still occurred in the troughs, and the onset of stall caused the pressure contours to no longer be as smooth. Quantitatively, when α was increased from 8 to 12°, the magnitude of pressure in the trough increased 257%. At $\alpha = 16°$, it was seen that there were now regions near the tip of the flipper where the pressure contours were no longer uniform. Again, the lowest global value of pressure occurred in the troughs. The numeric value of pressure in the second trough actually increased at this α, which is due to flow separation effects influencing the flow near the LE. In the deep-stall region of $\alpha = 20°$, the pressure distribution on the surface of the flipper was seen to be generally nonuniform, as unsteady flow separation had caused an uneven distribution of the pressure. The fact that the lowest global value of pressure occurred in the troughs for all α is in agreement with an experimental water-tunnel study performed on rudders with tubercles, where it was found that cavitation (which indicates a region of low pressure) first occurred in the troughs [11].

For the smooth flipper at the low, nonstall α of 4 and 8°, the pressure contours were again seen to be smooth and generally ran spanwise along the flipper (Fig. 8). When α was increased to 12°, which is not yet in the stall region but nearing the maximum C_L, the pressure contours were still smooth and ran spanwise along the flipper, although the pressure gradient along the leading edge of the flipper was seen to markedly increase. At $\alpha = 16°$, which corresponds to stall for the smooth flipper, a large low-pressure area was seen along the leading edge of the flipper. Additionally, the pressure distribution was no longer smooth along the trailing edge of the flipper, with flow separation causing large regions of uneven pressure distribution.

C. Differences in Sectional Pressure Coefficient

The CFD results were used to plot the sectional pressure coefficient C_P for both the smooth and tubercle flippers, and the results are shown in Fig. 9. The cross sections chosen for the tubercle flipper were located at spanwise coordinates y corresponding to the second trough from the tip and the sixth bump from the root. The cross section chosen for the smooth flipper was located at a y corresponding to the same y as the tubercle trough. The α chosen was 16°, which was in the stall region for the smooth flipper and near $C_{L,\max}$ for the tubercle flipper.

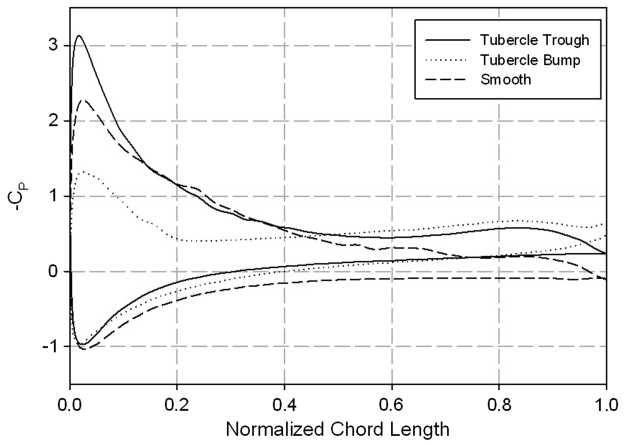

Fig. 9 Sectional coefficient of pressure, C_P, plots for the smooth and tubercle flippers. Results were generated using SFS.

Figure 9 shows that the peak absolute value of C_P occurred for the tubercle trough, followed by the smooth flipper and then the tubercle bump. As discussed previously, localized upwash in the trough regions, caused by the formation of a leading-edge vortex on the upper (suction) surface of the tubercle, generated more severe adverse pressure gradients in the troughs, which corresponds to the C_P differences seen in Fig. 9. The differing stall patterns between the smooth and tubercle flipper were also seen to cause differences in the C_P distribution, especially along a normalized chord length of ~0.5 to the TE.

VII. Conclusions

In this study, flow simulations of two different models based on the humpback whale flipper, one with a smooth leading edge and one with simulated tubercles along its leading edge, were conducted and compared with previously obtained experimental results. Two different commercial CFD codes, STAR-CCM+ and SolidWorks Flow Simulation 2009, were used for the flow simulations. STAR-CCM+ was found to give results that were in better agreement with experiment in the nonstall region and SFS was found to give results that were in better agreement with experiment in the stall region, although each code had its own advantages and disadvantages. In general, predictions for both codes in the nonstall region tended to be very good in terms of lift, and STAR-CCM+ performed better in terms of drag due to implementation of the Spalart–Allmaras turbulence model. In the stall region, lift predictions were better with SFS, while drag predictions were problematic for both codes (although SFS performed slightly better). Flow visualizations confirmed different stall patterns between the two flippers, with the smooth flipper exhibiting primarily trailing-edge stall and the tubercle flipper tending to stall in the troughs of the tubercles first. Pressure contours were also different, with the tubercle flipper exhibiting low pressures and large pressure gradients in the troughs. Flow visualization also showed that the tubercle flipper is able to obtain a larger C_L poststall due to regions of the flow remaining attached along the flipper span, due to the tubercles.

This study has also shown certain limitations of CFD codes that implement the RANS equations as they apply to this problem. The dynamics of the turbulent fluid flow around the flippers in this study were exceedingly complex and included such factors as low-Reynolds-number effects and detached, coherent vortex interaction. Use of RANS to predict the flow may therefore risk neglecting phenomena that have a first-order impact on lift and drag mechanisms. This was seen by the fact that the drag predictions tended to be of lower quality than lift predictions, and poststall predictions that involved the effects of detached vortices were problematic. Alternate numerical methods such as the detached eddy simulation model used by Pedro and Kobayashi [13] have the advantage of increased accuracy in the stall region, but also have the disadvantage of extreme computational cost compared with RANS. Therefore, the researcher must take into account accuracy desired, complexity of the flowfield (i.e., region of flow and stall vs nonstall), and availability of computational resources (both memory and time) when deciding which numerical solution method to use. Overall, although CFD can be a very useful tool for explaining experimental results, it must be used with care as not all predictions were found to be entirely accurate when compared with experiment.

Acknowledgments

The authors wish to thank the technical support staff of the U.S. Naval Academy Subsonic Wind Tunnel Laboratory. P. W. W. was supported by the National Defense Science and Engineering Graduate Fellowship through the U.S. Office of Naval Research. L. E. H. and M. M. M. received support from the National Science Foundation.

References

[1] Fish, F. E., and Battle, J. M., "Hydrodynamic Design of the Humpback Whale Flipper," *Journal of Morphology*, Vol. 225, 1995, pp. 51–60.

doi:10.1002/jmor.1052250105
[2] Woodward, B. L., Winn, J. P., and Fish, F. E., "Morphological Specializations of Baleen Whales Associated with Hydrodynamic Performance and Ecological Niche," *Journal of Morphology*, Vol. 267, 2006, pp. 1284–1294. doi:10.1002/jmor.10474
[3] Fish, F. E., and Lauder, G. V., "Passive and Active Flow Control by Swimming Fishes and Mammals," *Annual Review of Fluid Mechanics*, Vol. 38, 2006, pp. 193–224. doi:10.1146/annurev.fluid.38.050304.092201
[4] Watts, P., and Fish, F. E., "The Influence of Passive, Leading Edge Tubercles on Wing Performance," *Proceedings of the Unmanned Untethered Submersible Technology (UUST01)*, 2001.
[5] Miklosovic, D. S., Murray, M. M., Howle, L. E., and Fish, F. E., "Leading-Edge Tubercles Delay Stall on Humpback Whale (*Megaptera novaeangliae*) Flippers," *Physics of Fluids*, Vol. 16, No. 5, 2004, pp. L39–L42. doi:10.1063/1.1688341
[6] Miklosovic, D. S., Murray, M. M., and Howle, L. E., "Experimental Evaluation of Sinusoidal Leading Edges," *Journal of Aircraft*, Vol. 44, No. 4, 2007, pp. 1404–1408. doi:10.2514/1.30303
[7] Stein, B., and Murray, M. M., "Stall Mechanism Analysis of Humpback Whale Flipper Models," *Proceedings of the Unmanned Untethered Submersible Technology (UUST05)*,, 2005.
[8] Johari, H., Henoch, C., Custodio, D., and Levshin, A., "Effects of Leading-Edge Protuberances on Airfoil Performance," *AIAA Journal*, Vol. 45, 2007, pp. 2634–2642. doi:10.2514/1.28497
[9] Murray, M. M., Miklosovic, D. S., Fish, F. E., and Howle, L. E., "Effects of Leading Edge Tubercles on a Representative Whale Flipper Model at Various Sweep Angles," *Proceedings of the 14th International Symposium on Unmanned Untethered Submersible Technology*, Durham, NH, 2005.
[10] van Nierop, E. A., Alben, S., and Brenner, M. P., "How Bumps on Whale Flippers Delay Stall: An Aerodynamic Model," *Physical Review Letters*, Vol. 100, 2008, Paper 054502. doi:10.1103/PhysRevLett.100.054502
[11] Weber, P. W., Howle, L. E., and Murray, M. M., "Lift, Drag and Cavitation Onset on Rudders with Leading Edge Tubercles," *Marine Technology and SNAME News*, Vol. 47, 2010, pp. 27–36.
[12] Stanway, M. J., "Hydrodynamic Effects of Leading-edge Tubercles on Control Surfaces and in Flapping Foil Propulsion," Master's Thesis, Department of Mechanical Engineering, Massachusetts Inst. of Technology, Cambridge, MA, 2008.
[13] Pedro, H. T. C., and Kobayashi, M. H., "Numerical Study of Stall Delay on Humpback Whale Flippers," 46th AIAA Aerospace Sciences Meeting and Exhibit, AIAA Paper 2008-0584, Reno, NV, 2008.
[14] STAR-CCM+, Software Package, Ver. 4.02, CD-Adapco, New York, 2009.
[15] SolidWorks Flow Simulation, Software Package, Ver. 2009, Dassault Systemes SolidWorks Corp., Concord, MA, 2009.
[16] Barlow, J. B., Rae, W. H., and Pope, A., *Low-Speed Wind Tunnel Testing*, 3rd ed., Wiley, New York, 1999, pp. 367–425.
[17] SolidWorks, Software Package, Ver. 2009, Dassault Systemes SolidWorks Corp., Concord, MA, 2009.
[18] Pope, S. B., *Turbulent Flows*, Cambridge Univ. Press, Cambridge, England, U.K., 2000, pp. 383–386.